Controlled lateral anisotropy in correlated manganite heterostructures by interface-engineered oxygen octahedral coupling

Z. Liao[1], M. Huijben[1]★, Z. Zhong[2], N. Gauquelin[3], S. Macke[4,5], R. J. Green[4,6], S. Van Aert[3], J. Verbeeck[3], G. Van Tendeloo[3], K. Held[2], G. A. Sawatzky[4], G. Koster[1] and G. Rijnders[1]

Controlled in-plane rotation of the magnetic easy axis in manganite heterostructures by tailoring the interface oxygen network could allow the development of correlated oxide-based magnetic tunnelling junctions with non-collinear magnetization, with possible practical applications as miniaturized high-switching-speed magnetic random access memory (MRAM) devices. Here, we demonstrate how to manipulate magnetic and electronic anisotropic properties in manganite heterostructures by engineering the oxygen network on the unit-cell level. The strong oxygen octahedral coupling is found to transfer the octahedral rotation, present in the NdGaO$_3$ (NGO) substrate, to the La$_{2/3}$Sr$_{1/3}$MnO$_3$ (LSMO) film in the interface region. This causes an unexpected realignment of the magnetic easy axis along the short axis of the LSMO unit cell as well as the presence of a giant anisotropic transport in these ultrathin LSMO films. As a result we possess control of the lateral magnetic and electronic anisotropies by atomic-scale design of the oxygen octahedral rotation.

Emergent phenomena in oxide heterostructures[1,2], such as interface charge transfer[3], two-dimensional free electron gases[4] and ferromagnetism between two non-magnetic materials[5], are induced by the dedicated coupling between spin, orbital, charge and lattice degrees of freedom[6,7]. Developing strategies to engineer these intimate couplings in oxide heterostructures is crucial to uncover new phenomena and pave the path towards novel functionalities with atomic-scale dimensions. Polar discontinuity[4], inducing strain[8–10], charge transfer[3], and spatial confinement[11,12] are several well-known strategies. In ABO$_3$ perovskites, orbital, charge and spin order are intimately correlated with the BO$_6$ oxygen octahedra[13–20]. In the bulk, the oxygen octahedral rotation (OOR) and deformation are usually controlled by isovalent substitution or by the deployment of high pressure[13–19], but oxide heterostructures offer additional ways to tune the lattice structure[1,2,10,20–24]. The OOR can be tailored either by strain or interfacial oxygen octahedral coupling (OOC; refs 23–27). The OOC is a geometric constraint effect which forces the octahedra in a film to rotate to retain corner connectivity of oxygen octahedra across an interface[23].

For decades, strain has been used for heterostructure engineering, but strain is usually a long-range effect depending on lattice mismatch[28], and therefore less controllable at the atomic scale, limiting its application towards complex devices where films with varying local properties on a single wafer are required. The OOC, which unlike strain has a short impact length scale of ∼2 nm (refs 23–27), could be a new route to realize atomic-scale control of material properties and functionalities. However, questions are still open whether the OOC can compete with strain, how strong an impact it can make on the functionalities and if it can transfer not
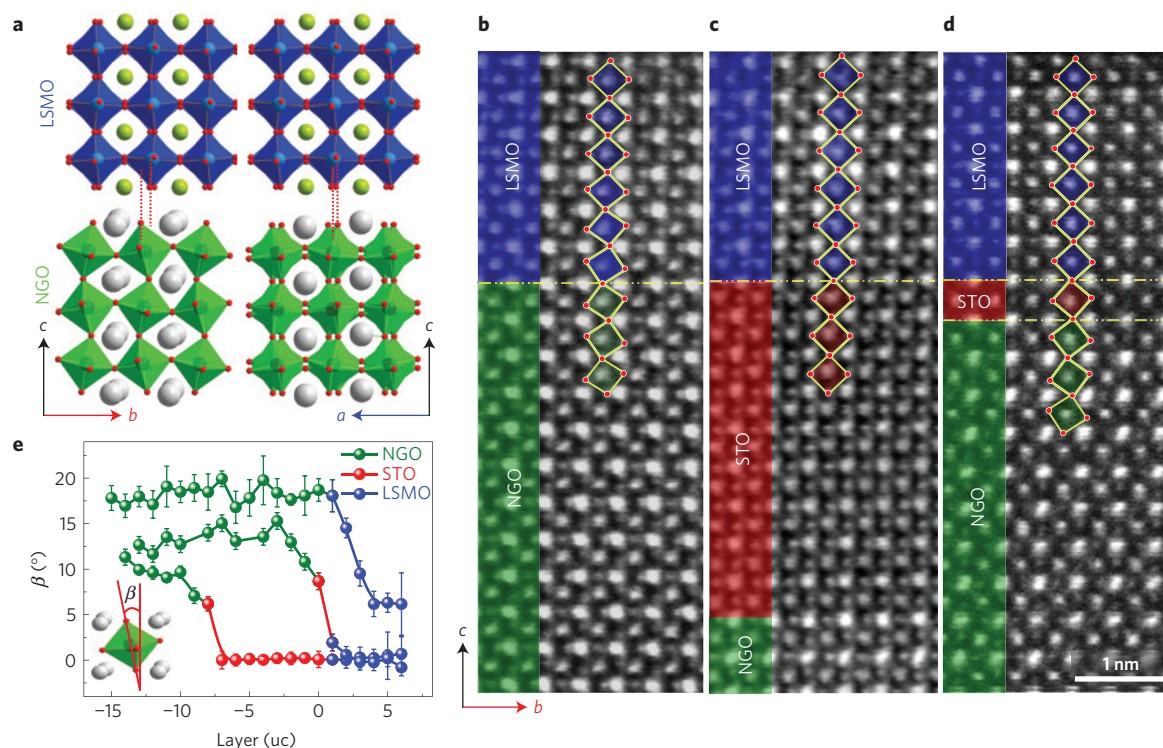
only the magnitude of rotation but also the Glazer rotation pattern[29] to a film. Such controllable OOR will provide a feasible new route to the artificial design of structures with novel functionalities.

By utilizing the OOC at the LSMO and NGO (110) interface, we demonstrate the possibility of transferring the characteristic NGO anisotropic structure into epitaxial LSMO films. This in turn creates not only new but also switchable magnetic and electronic anisotropies. The rhombohedral LSMO possesses an $a^-a^-a^-$ rotation, which results in an isotropic B-O-B bond angle (θ) and isotropic properties[16]. The Glazer symbol[29] here and after corresponds sequentially to the rotation along a, b and c axis respectively. In contrast, the orthorhombic NGO possesses an $c^+a^-a^-$ rotation with a larger θ along the [001] direction than along the [1$\bar{1}$0] direction[30]. For convenience, pseudo-cubic indices are used for NGO, with a, b and c corresponding to [001], [1$\bar{1}$0] and [110], respectively. The structural characteristics of LSMO and NGO give rise to in-phase versus out-of-phase rotation type mismatch occurring along the a-axis (see left panel of Fig. 1a), whereas both are out-of-phase along the b-axis (see right panel of Fig. 1a). The magnitude of the bond angle θ also has a certain degree of mismatch: ∼154° in NGO versus 166.3° in LSMO. As a result, both the anisotropic rotation type mismatch and the large difference (∼12°) in bond angle will cause a strong discontinuity of the octahedra (see Fig. 1a). Therefore, the oxygen atoms need to rearrange at the interface, resulting in a large change of the OOR in the LSMO film.

The effect of the OOC at the LSMO/NGO interface is visualized by atomically resolved Cs-corrected scanning transmission electron microscopy (STEM). Thin LSMO films have been grown by pulsed laser deposition on NGO (110) substrates[31] (see Methods and

Figure 1 | Oxygen octahedral coupling at interfaces in manganite heterostructures. a, Schematic models of atomic ordering in LSMO and NGO crystal structures. **b–d**, Inversed annular bright-field STEM images of LSMO/NGO (**b**), LSMO/STO (9 uc)/NGO (**c**) and LSMO/STO (1 uc)/NGO (**d**) heterostructures. The oxygen atoms are clearly visible, and the connectivity of oxygen octahedra across the interfaces is indicated. All the LSMO films are 6 uc thick. **e**, Layer-position-dependent mean octahedral tilt angle (β) together with its standard deviation in LSMO/NGO heterostructures with and without a STO buffer layer. The data for the non-buffered sample are shifted upwards by 6° for clarity.

Supplementary Fig. 1). All films are fully strained to NGO (see Supplementary Fig. 2), resulting an overall ∼0.4% compressive strain on LSMO with 0.2% in-plane anisotropy[16,30]. Atomic ordering and chemically sharp interfaces were achieved for the samples investigated in this article, as demonstrated by the atomic electron energy loss spectroscopy (EELS) maps (see Supplementary Fig. 3). The in-phase rotation along the a-axis enables us to directly visualize and quantify the BO_6 octahedral tilt in the bc plane through the annular bright-field STEM (ABF-STEM) image (see Fig. 1b; refs 27,32). The LSMO strongly follows the NGO rotation characteristic and becomes in-phase along the a-axis, which in bulk LSMO is out-of-phase. Close to the interface, the MnO_6 octahedral tilt angle is comparable to that of GaO_6, as shown by the depth profile of the BO_6 tilt angle across the interface in Fig. 1e (for estimation of the tilt angle, see Supplementary Fig. 4). The tilt angle changes continuously from the GaO_6 substrate value to bulk MnO_6 (far from interface). Interestingly, the first 2 uc layers of LSMO have almost the same tilt angle as NGO. The impact of the octahedral coupling decays rapidly away from the interface and disappears above 4 uc layers. Therefore, the OOC at the LSMO/NGO interface results in the alteration of the OOR (in-phase, out-of-phase) of the LSMO close to the interface, in which the magnitude of the tilt angle is comparable to that of NGO (Fig. 1b). Because of the short impact length scale of the OOC, the OOR of the LSMO can be significantly altered by inserting a non-tilted $SrTiO_3$ (STO) buffer layer (Fig. 1c). Within the STO layer, the OOR is also coupled to the OOR of NGO, but the tilt angle relaxes quickly—that is, the tilt of TiO_6 octahedra starts to disappear above 2 uc layers. Consequently, the LSMO connects to a non-tilted OOR and shows no evidence, within the STEM spatial resolution, of tilting of the MnO_6 octahedra from the first layer (see Fig. 1e). Owing to the steep decay of tilt in STO, a 1 uc STO buffer layer is found to be thick enough to significantly

reduce the tilt in LSMO (see Fig. 1d,e). Together with non-buffered LSMO, the resulting interface structure of LSMO indicates that the local OOR at the substrate surface acts as a controllable template for the structure of the epitaxial LSMO film.

The observed interfacial OOC has a marked impact on the magnetic properties. The 9 uc STO buffer layer reduces the octahedral tilt in LSMO, thus enhancing the magnetism—that is, a 9 uc STO buffer layer increases the Curie temperature (T_C) of the 6 uc LSMO from 145 K to 240 K. The enhancement is already found when using a 1 uc STO buffer layer, as the 6 uc LSMO film exhibits a T_C of 180 K, consistent with the observed reduced tilt in LSMO by the 1 uc STO buffer layer (see Fig. 1d). The saturated magnetic moment of such STO-buffered LSMO is also larger than the non-buffered LSMO film (see Fig. 2a–c).

Beyond the enhancement, a more striking phenomenon is switching of the magnetic anisotropy (MA) by engineering the interfacial OOR. Owing to the different OOR pattern, the 6 uc thick LSMO films with or without the STO buffer layer have a different magnetization easy axis, although both exhibit uniaxial MA. The easy axis of the non-buffered LSMO is the a-axis, as shown in Fig. 2a, in strong contrast to the observed b-axis easy axis in thick LSMO films[31,33]. When inserting a STO buffer layer with a thickness ranging from 1 uc to 36 uc (LSMO/STO/NGO), the easy axis is again switched to the b-axis. The magnetic behaviour of 6 uc LSMO films on top of a 1 uc STO and 9 uc STO buffer layer is shown as examples in Fig. 2b and c, respectively. For convenience, the MA with an easy axis along the short axis a is defined as interfacial MA (IMA), whereas an easy axis along the long axis b is defined as bulk MA (BMA). Comparison between the structure of LSMO with and without the STO buffer layer indicates that the IMA is correlated with the strong tilted LSMO structure, whereas the BMA comes from the nearly non-tilted (NNT) structure. A single unit-cell
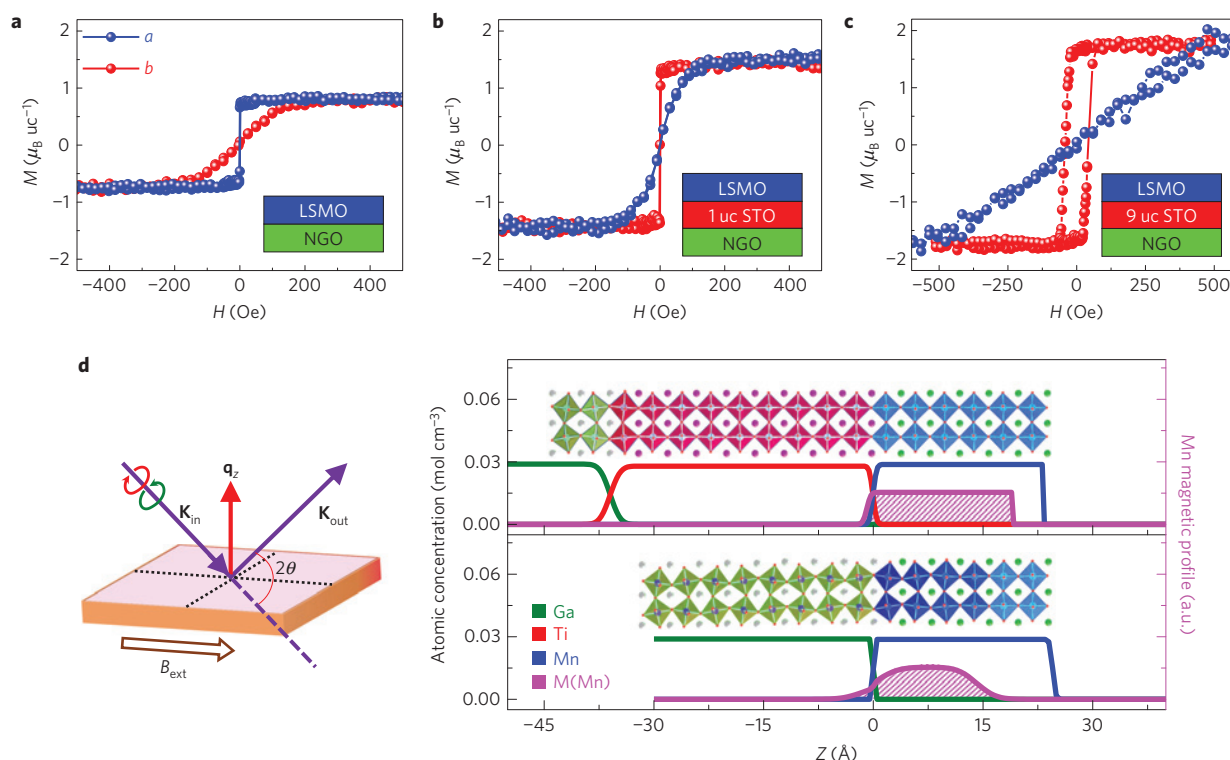
Figure 2 | Magnetic anisotropy in manganite heterostructures. a–c, $M–H$ curves at 100 K along the a- and b-axis of the 6 uc LSMO films on NGO substrates without (**a**) and with a 1 uc (**b**) and 9 uc (**c**) STO buffer layer. **d**, RXR measurements of 6 uc LSMO films with (top panel) and without (bottom panel) a 9 uc STO buffer layer showing depth profiles of the Ga, Ti, Mn atomic concentration (green, red and blue lines, respectively) and Mn magnetization (M, purple line with shaded area) at 20 K. The schematic on the left shows the experimental set-up used to perform RXR measurements, where a 0.6 T magnetic field was applied in-plane along the magnetic easy axis during the measurement. Atomic structure profiles along the out-of-plane direction (Z), corresponding to Fig. 1b,c, are also shown for comparison.

STO buffer layer is thick enough to reduce the tilt in LSMO, and thus to switch the easy axis of LSMO (see Figs 1d and 2b), indicating the capability to tune the anisotropic properties by atomic-scale control. By separating IMA and BMA with a STO barrier in LSMO/STO/LSMO/NGO magnetic tunnelling junctions, we are now able to realize orthogonal magnetizations between top and bottom LSMO electrodes (see Supplementary Fig. 5). Furthermore, patterning of the STO buffer layer now also allows us to artificially create in-plane magnetic domains (see Supplementary Fig. 5).

The depth profiles of the magnetization further confirm that IMA arises from the strongly tilted interface structure. The atomic concentration profile and magnetic depth profile in 6 uc LSMO films with and without the STO buffer layer have been probed by resonant X-ray reflectometry (RXR; ref. 34), as shown in Fig. 2d (for details of the RXR experiment, see Supplementary Fig. 6). A depth profile of Mn magnetization (M) can be obtained from the best fit of the asymmetric spectra between left- and right-circularly polarized light. The profiles of Ga, Ti and Mn atomic concentration are also shown for comparison and indicate an atomic sharp interface with negligible interfacial intermixing. The active magnetic layers in these two samples are all located at the interface region. Our magnetic profiles also reveal the presence of magnetic dead layers near the surface[35] for both buffered and non-buffered LSMO films. The OOC has an impact length scale of ~2 nm and, therefore, could have an influence on the surface part of our ultrathin LSMO films on NGO, which can be excluded for our thicker LSMO films. A more detailed analysis will be performed in a future study. Compared with the non-buffered LSMO, the less distorted buffered LSMO film exhibited a more uniform magnetism owing to the reduced structural distortion at the interface as well as a reduced thickness of the dead layer on the surface. This fact could explain the observed

enhanced saturated magnetization in buffered LSMO film, as shown in Fig. 2a–c. Interestingly, the active magnetic layer in the non-buffered LSMO is the ~3 uc interface region, and thus coincident with the strong tilted layer (see bottom panel of Fig. 2d). Therefore, the IMA is correlated with the strong tilted LSMO structure, whereas the BMA is coupled to NNT structure.

The distinct OOR patterns near and far from the interface region give rise to a sharp transition of the MA at 8 uc LSMO layer thickness, see Fig. 3. The contribution from the NNT part to the magnetic anisotropic energy (MAE) will increase with increasing thickness; hence, thicker films ($t > 8$ uc) exhibit BMA. The strong tilt part dominates in thinner films with $t < 8$ uc; hence, these films exhibit IMA. At 8 uc, the competition between IMA and BMA results in biaxial anisotropy, with the easy axis along ab and $-ab$ directions. The thickness dependence of LSMO thin films further indicates that IMA arises from an interfacial NGO-like OOR pattern, whereas the strain-dominated NNT part gives rise to BMA.

Concomitant with the MA, the electronic transport properties in the LSMO films are also found to exhibit anisotropies with a sharp transition at a thickness of 8 uc. Besides a thickness-dependent metal insulator transition[36], an interfacial OOC-driven giant transport anisotropy is also observed in LSMO films with thicknesses of 6 and 7 uc, which exhibit higher electrical conductivities along the a-axis, see Fig. 4a. In thicker films, where the OOC subsides, the anisotropy becomes much smaller. No thermal hysteresis is observed in the cooling down and warming up cycles, therefore possible anisotropic percolation in a phase separation scenario is excluded[9]. Figure 4b shows the resistivity along two different directions, a and b, at 50 K. Almost two orders of magnitude difference of resistivity between the two directions is observed in the 6 uc sample, significantly larger than previously reported strain-induced
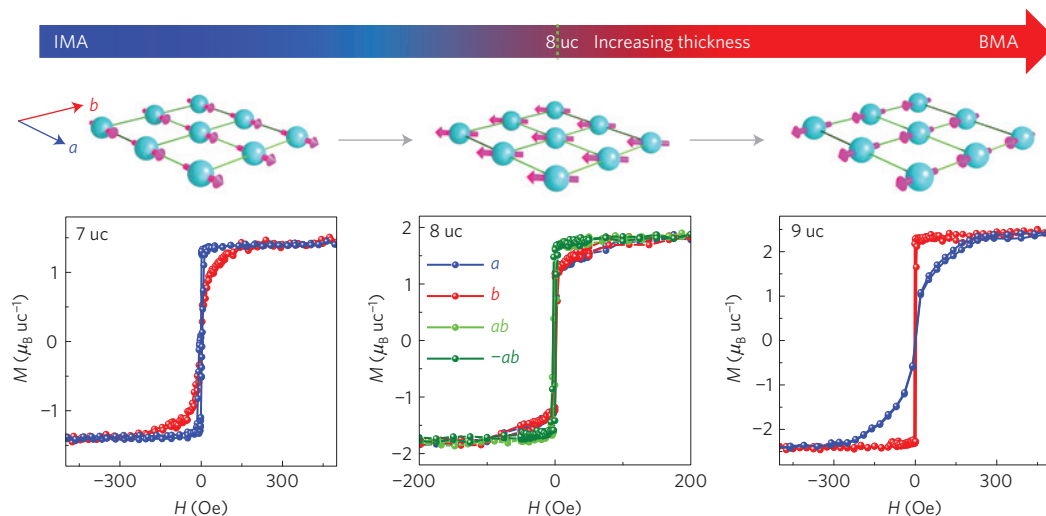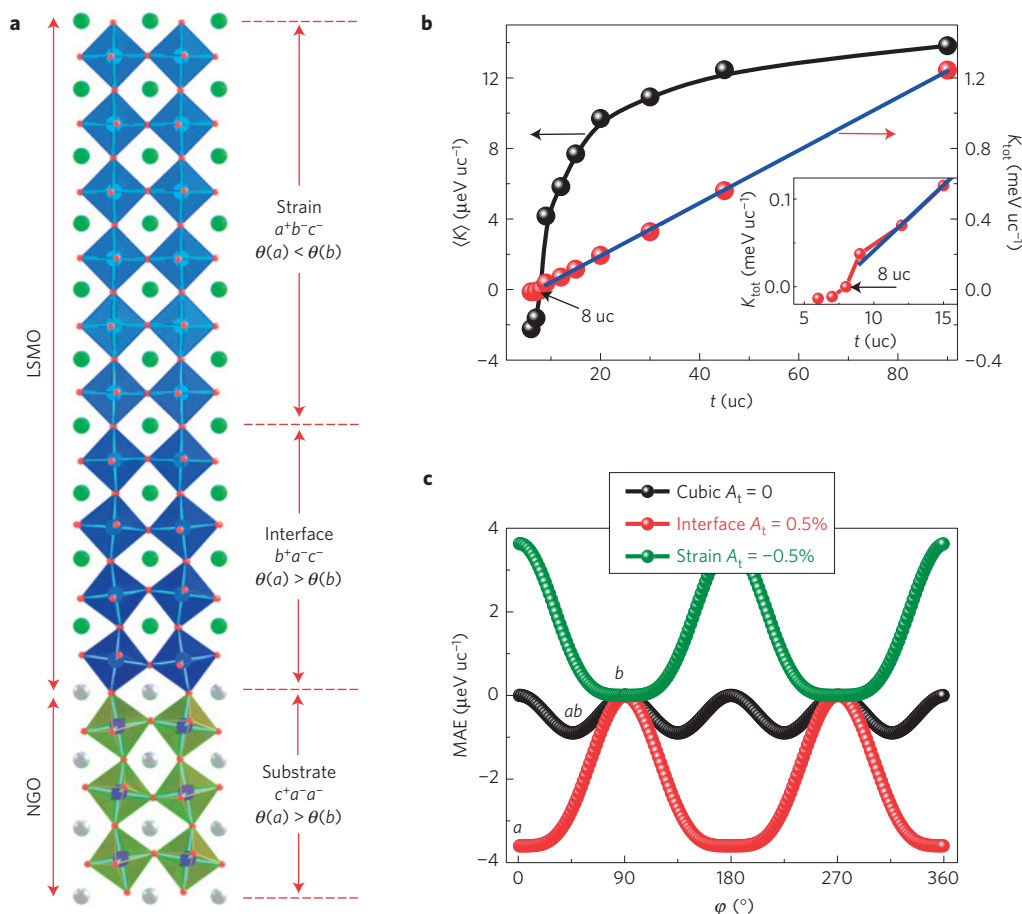
Figure 3 | Thickness dependence of the magnetic anisotropy in manganite heterostructures. M–H curves at 100 K along the a- and b-axis of LSMO films with thicknesses of 7, 8 and 9 uc on NGO substrates. The schematics at the top show the corresponding ground state of the Mn spin orientation.
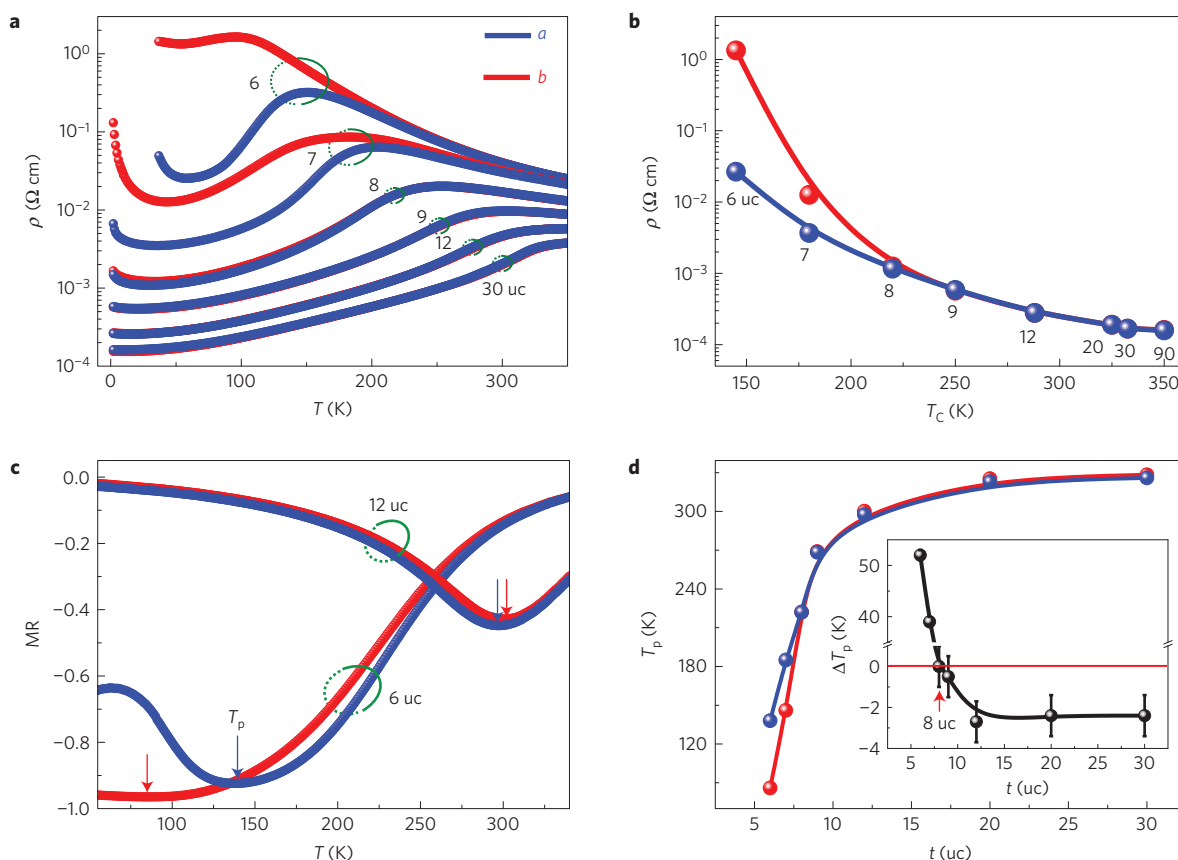
Figure 4 | Thickness dependence of the transport anisotropy in manganite heterostructures. a, Temperature-dependent resistivity along the a- and b-axis for different LSMO thicknesses from 6 to 30 uc. Resistivity curves for the same thickness are grouped by the green circles. **b**, Curie-temperature-dependent resistivity at 50 K along the a- and b-axis. The corresponding thickness is marked at each data point. **c**, Temperature-dependent magnetoresistance MR $= (R(B) - R(0))/R(0)$ along the a- and b-axis under out-of-plane 9 T magnetic field for 6 and 12 uc LSMO films. Resistivity curves for the same thickness are grouped by the green circles. The arrows indicate the position of T_p. **d**, T_p versus LSMO film thickness along the a- and b-axis. Inset, $\Delta T_p = T_p(a) - T_p(b)$ versus LSMO film thickness. The error bars are temperature uncertainty due to the temperature ramping step length. Data measured along the a-axis are indicated in blue in all four figures, whereas data along the b-axis are indicated in red.

transport anisotropy[37] in LSMO/DyScO$_3$. This difference decreases with increasing thickness, and, for $t \geq 8$ uc, this difference is too small to note any anisotropy. However, the temperature-dependent magnetoresistance, MR $= (R(B) - R(0))/R(0)$, in Fig. 4c still reflects

the presence of transport anisotropy in thick films. Both thin film (6 uc) and thick film (12 uc) exhibit an anisotropic MR effect with a peak position T_p, which reflects a metal-to-insulator transition in manganites (see Supplementary Fig. 7). However, the signs of

Figure 5 | Structural mechanism of directional switching of magnetic anisotropy. a, Structural evolution along the out-of-plane direction of the LSMO thin film on a NGO substrate. **b**, Film thickness dependence of the anisotropic energy constant $\langle K \rangle$ and total anisotropic energy constant K_{tot} at 50 K. The blue line is resultant linear fitting of K_{tot} versus t in the region $t > 8$ uc. Inset: zoom-in of the K_{tot} versus t curve including the linear fitting result around $t = 8$ uc. **c**, Tight-binding simulations of the anisotropy energy of a LSMO monolayer with different asymmetric hopping factor A_t ($= 1 - t_0(\mathbf{b})/t_0(\mathbf{a})$): 0% (cubic LSMO, black); 0.5% (interfacial LSMO on NGO, red); −0.5% (strained bulk LSMO on NGO, green).

$\Delta T_P = T_p(a) - T_p(b)$ for 6 uc and 12 uc films are opposite. Therefore, there is a switch of transport anisotropy with increasing thickness. As shown in Fig. 4d, the difference ΔT_P is thickness dependent and becomes zero at 8 uc. For $t < 8$ uc, it is reversed and as large as $\Delta T_P = 52$ K for 6 uc LSMO, whereas in films with $t > 8$ uc, it is only about −2 K. As the more conductive axis has higher T_P, and based on Figs 3 and 4d, we can conclude that the easy axis for electronic transport (more conductive axis) coincides with the magnetic easy axis of the LSMO films. By switching the magnetic easy axis of a 6 uc LSMO film by the introduction of a STO buffer layer, the transport easy axis is also switched to the b-axis (see Supplementary Fig. 7).

Let us now turn to the mechanism of the thickness-driven switch of the anisotropic properties. As strain does not change with thickness, and interfacial intermixing is negligible, the transition of MA with thickness can be expected to correlate with the OOR pattern. Along the a-axis, an in-phase (NGO) and out-of-phase (LSMO) mismatch would cause huge oxygen displacements to retain the connectivity of the oxygen octahedra. Furthermore, the rotation of MnO_6 octahedra along the a-axis causes the bond angle θ along the b-axis to become smaller. Although, along the b-axis, the OOR pattern for both LSMO and NGO are out-of-phase, the displacement of oxygen atoms necessary to match the substrate is less. As a result, the bond angle along the a-axis is larger than along the b-axis, $\theta(a) > \theta(b)$, which is further evidenced

by the STEM images of the LSMO/NGO cross-section with the zone axis along the b-axis (see Supplementary Figs 8 and 9). Further away from the interface, the OOC effect subsides and the strain dominates, resulting in $\theta(b) > \theta(a)$ (ref. 38). Based on the above consideration, a structural evolution of a LSMO film is shown schematically in Fig. 5a. The LSMO film is divided into two regions, the interface OOC-driven $b^+a^-c^-$ and the strain-induced[38] $a^+b^-c^-$. The larger rotation along the c-axis for both regions is due to LSMO in-plane compressive strain, which increases the rotation along the c-axis to give rise to a smaller in-plane lattice constant[38]. In the crossover thickness, the complete LSMO film can be averagely described by $a^+a^-c^-$ and $\langle\theta(a)\rangle \approx \langle\theta(b)\rangle$. The structure characteristic of LSMO near the interface is expected to cause an anisotropic bandwidth (w) according to the formula[39] $w \propto (\cos((\pi - \theta)/2)/d^{3.5})$, with $w(a) > w(b)$. Further away from the interface region, $\theta(b) > \theta(a)$ leads to $w(b) > w(a)$. The expected changes of anisotropic bond angle and bandwidth are consistent with our observed anisotropic transport properties within the double exchange model[40].

According to Fig. 1b, the lattice structure of LSMO films relaxes with thickness and becomes bulk-like at a thickness of about 4 uc. Therefore, in thick LSMO films we expect the presence of two regions: an interface region where the anisotropic properties in each layer change with layer position, and a strain-dominated bulk region where the anisotropic properties are less dependent on

layer position. The uniaxial MAE is described by $E = K_u \cos^2\varphi$, where φ is an in-plane angle relative to the a-axis. For uniaxial anisotropy $K_u = E(a) - E(b)$ is positive or negative, indicating that the easy axis is the b or a-axis, respectively; for biaxial anisotropy $K_u = 0$. The total K_u can be expressed by $K_{tot} = \sum_{n=1}^{t} K_u(n)$, where $K_u(n)$ is the MAE constant of the nth layer. The mean MAE constant $\langle K \rangle (= K_{tot}/t)$ (for measurement of $\langle K \rangle$, see Supplementary Fig. 10) is found to depend nonlinearly on thickness (see Fig. 5b). The value of $\langle K \rangle$ exhibits a clear thickness dependence and a crossover transition from positive to negative values, which can be observed at 8 uc. In contrast, K_{tot} is linearly dependent on thickness when $t > 8$ uc (see Fig. 5b). Therefore, K_{tot} can be rewritten as $K_{tot} = \sum_{n=1}^{t_I} K_u(n) + K_{uB}(t - t_I) = K_{uB}t - c$. Here, t_I is the thickness of interface region beyond which the $K_u(n)$ is approximated to be constant at K_{uB} and c is a constant. K_{uB} and c, as obtained from linear fitting of the K_{tot} versus t curve at $t > 8$ uc, are 14.4 μeV uc^{-1} and 103.7 μeV uc^{-1}, respectively. With these parameters, a critical thickness (t_c), where these sub-layers do not contribute to $K_{tot}(K_{uB}t_c - c = 0)$, can be estimated to be 7.2 uc, in good agreement with the observed 8 uc critical thickness for $\langle K \rangle = 0$ as determined by the MA measurements.

To understand the microscopic origin of the MA and the expected coupling between transport and MA, we construct by means of density functional theory (DFT) a tight-binding Hamiltonian of LSMO ultrathin films: $\sum_R t_{\alpha\beta}(\mathbf{R})e^{i\mathbf{K}\cdot\mathbf{R}} + (\lambda/2)\sigma(\theta,\varphi) + \xi L \cdot S$ (see Supplementary Figs 11 and 12). Here, $t_{\alpha\beta}(\mathbf{R})$ represents the hopping integral from orbital α at site 0 to orbital β at site $\mathbf{R}$. The structural change due to OOC and strain mainly affects $t_{\alpha\beta}(\mathbf{R})$, which in turn leads to a change in the MAE. The hopping terms $t_{\alpha\beta}(\mathbf{R})$ can be qualitatively indicated by the transport properties in our experiment. We therefore simply mimic the structural and transport anisotropy by introducing anisotropic hopping terms[40] parametrized by A_t: $t_0(\mathbf{a})$ and $t_0(\mathbf{b}) = t_0(\mathbf{a})(1 - A_t)$ along $\mathbf{a}$ and $\mathbf{b}$ respectively. The calculation of the MAE indicates an in-plane easy axis for a monolayer LSMO film (see Supplementary Fig. 12), whereas the easy axis in the ab-plane depends on the asymmetric hopping factor A_t (see Fig. 5c). In the case of an isotropic in-plane structure ($A_t = 0$), a biaxial anisotropy with easy axis $[110]_{pc}$ is obtained consistent with observations in (001) LSMO films on cubic STO and (LaAlO$_3$)$_{0.3}$(Sr$_2$AlTaO$_6$)$_{0.7}$ substrates (see Supplementary Fig. 13). If $t_0(\mathbf{a})$ is 0.5% higher than $t_0(\mathbf{b})$ ($A_t = 0.5\%$), the easy axis is rotated from the ab direction to the a-axis and the film becomes uniaxially anisotropic, whereas $A_t = -0.5\%$ will switch the easy axis to the b-axis. Thus, the easy axis prefers to align along the axis with the largest hopping amplitude, which is also the axis for the largest conductivity, as in experiment. The calculated in-plane anisotropic energy is of the order of 4 μeV uc^{-1}, qualitatively consistent with the experimental observations.

In conclusion, OOC-driven magnetic and transport anisotropies are realized in LSMO/NGO heterostructures. Competition between the interfacial OOC and the strain further away from the interface leads to a thickness-driven sharp transition of the anisotropic properties. The observed coupling of transport and MA, as well as the tight-binding modelling, indicate the key role of the anisotropic bandwidth for the anisotropic properties in LSMO. Our finding will also provide new insights into the recently reported strain-driven transport anisotropy in manganite films[9,37,40]. The observed OOC can be extended to other perovskite oxide heterostructures or superlattices. Furthermore, the revealed competition between OOC and strain which results in thickness-dependent properties should have significant impact on the understanding of a widely reported reduced dimensionality effect in many correlated perovskite ultrathin films.

Our results unequivocally link the atomic structure near interfaces to macroscopic properties. The strong correlation between the controllable oxygen network and functionalities will have a significant impact on both fundamental research and the technological applications of correlated perovskite heterostructures. By controlling interfacial OOC, we are now able to pattern the magnetization in three dimensions to achieve non-collinear magnetization in both in-plane and out-of-plane directions, thus making these heterostructures promising for application in orthogonal spin-transfer devices, spin oscillators and low-field sensors[41,42]. Moreover, one could extend the revealed competition between strain and OOC to a new direction to realize piezoelectric control of magnetization reversal for spintronics applications by tuning the balance between these two co-existent effects.

Note added in proof: After this manuscript was accepted we noticed the work by another group also reporting control of the oxide-interface properties by interface engineering[43].

Methods

Methods and any associated references are available in the online version of the paper.

References

1. Hwang, H. Y. *et al*. Emergent phenomena at oxide interfaces. *Nature Mater.* **11**, 103–113 (2012).
2. Zubko, P., Gariglio, S., Gabay, M., Ghosez, P. & Triscone, J.-M. Interface physics in complex oxide heterostructures. *Annu. Rev. Condens. Matter Phys.* **2**, 141–165 (2011).
3. Chakhalian, J. *et al*. Orbital reconstruction and covalent bonding at an oxide interface. *Science* **318**, 1114–1117 (2007).
4. Ohtomo, A. & Hwang, H. Y. A high-mobility electron gas at the LaAlO$_3$/SrTiO$_3$ heterointerface. *Nature* **427**, 423–426 (2004).
5. Brinkman, A. *et al*. Magnetic effects at the interface between non-magnetic oxides. *Nature Mater.* **6**, 493–496 (2007).
6. Tokura, Y. & Nagaosa, N. Orbital physics in transition-metal oxides. *Science* **288**, 462–468 (2000).
7. Dagotto, E. Complexity in strongly correlated electronic systems. *Science* **309**, 257–262 (2005).
8. Aetukuri, N. B. *et al*. Control of the metal–insulator transition in vanadium dioxide by modifying orbital occupancy. *Nature Phys.* **9**, 661–666 (2013).
9. Ward, T. Z. *et al*. Elastically driven anisotropic percolation in electronic phase-separated manganites. *Nature Phys.* **5**, 885–888 (2009).
10. Schlom, D. G. *et al*. Strain tuning of ferroelectric thin films. *Annu. Rev. Mater. Res.* **37**, 589–626 (2007).
11. Boris, A. V. *et al*. Dimensionality control of electronic phase transitions in nickel-oxide superlattices. *Science* **332**, 937–940 (2011).
12. King, P. D. C. *et al*. Atomic-scale control of competing electronic phases in ultrathin LaNiO$_3$. *Nature Nanotech.* **9**, 443–447 (2014).
13. Salamon, M. B. & Jaime, M. The physics of manganites: structure and transport. *Rev. Mod. Phys.* **73**, 583–628 (2001).
14. Coey, J. M. D., Viret, M. & von Molnár, S. Mixed-valence manganites. *Adv. Phys.* **48**, 167–293 (1999).
15. Chmaissem, O. *et al*. Relationship between structural parameters and the Néel temperature in Sr$_{1-x}$Ca$_x$MnO$_3$ ($0 < \sim x < \sim 1$) and Sr$_{1-y}$Ba$_y$MnO$_3$ ($y < \sim 0.2$). *Phys. Rev. B* **64**, 134412 (2001).
16. Radaelli, P. G. *et al*. Structural effects on the magnetic and transport properties of perovskite A$_{1-x}$A$'_x$MnO$_3$ ($x = 0.25, 0.30$). *Phys. Rev. B* **56**, 8265–8276 (1997).
17. Alonso, J. A., Martínez-Lope, M. J., Casais, M. T., Aranda, M. A. G. & Fernández-Díaz, M. T. Metal–insulator transitions, structural and microstructural evolution of RNiO$_3$ (R = Sm, Eu, Gd, Dy, Ho, Y) perovskites: evidence for room-temperature charge disproportionation in monoclinic HoNiO$_3$ and YNiO$_3$. *J. Am. Chem. Soc.* **121**, 4754–4762 (1999).
18. Garcia-Munoz, J. L., Fontcuberta, J., Suaaidi, M. & Obradors, X. Bandwidth narrowing in bulk L$_{2/3}$A$_{1/3}$MnO$_3$ magnetoresistive oxides. *J. Phys. Condens. Matter* **8**, L787–L794 (1996).
19. Ding, Y. *et al*. Pressure-induced magnetic transition in manganite (La$_{0.75}$Ca$_{0.25}$MnO$_3$). *Phys. Rev. Lett.* **102**, 237201 (2009).
20. Zhai, X. F. *et al*. Correlating interfacial octahedral rotations with magnetism in (LaMnO$_3 + \delta$)N/(SrTiO$_3$)N superlattices. *Nature Commun.* **5**, 4283 (2014).
21. Rondinelli, J. M. & Spaldin, N. A. Structure and properties of functional oxide thin films: insights from electronic-structure calculations. *Adv. Mater.* **23**, 3363–3381 (2011).

22. Lee, J. H. *et al*. Dynamic layer rearrangement during growth of layered oxide films by molecular beam epitaxy. *Nature Mater.* **13,** 879–883 (2014).
23. Rondinelli, J. M., May, S. J. & Freeland, J. W. Control of octahedral connectivity in perovskite oxide heterostructures: an emerging route to multifunctional materials discovery. *MRS Bull.* **37,** 261–270 (2012).
24. Kinyanjui, M. K. *et al*. Lattice distortions and octahedral rotations in epitaxially strained $LaNiO_3/LaAlO_3$ superlattices. *Appl. Phys. Lett.* **104,** 221909 (2014).
25. Borisevich, A. Y. *et al*. Suppression of octahedral tilts and associated changes in electronic properties at epitaxial oxide heterostructure interfaces. *Phys. Rev. Lett.* **105,** 087204 (2010).
26. He, J., Borisevich, A. Y., Kalinin, S. V., Pennycook, S. J. & Pantelides, S. T. Control of octahedral tilts and magnetic properties of perovskite oxide heterostructures by substrate symmetry. *Phys. Rev. Lett.* **105,** 227203 (2010).
27. Aso, R., Kan, D., Shimakawa, Y. & Kurata, H. Atomic level observation of octahedral distortions at the perovskite oxide heterointerface. *Sci. Rep.* **3,** 2214 (2013).
28. Chen, Y. B. *et al*. Interface structure and strain relaxation in $BaTiO_3$ thin films grown on $GdScO_3$ and $DyScO_3$ substrates with buried coherent $SrRuO_3$ layer. *Appl. Phys. Lett.* **91,** 252906 (2007).
29. Glazer, A. M. Classification of tilted octahedral in perovskites. *Acta Crystallogr. B* **28,** 3384–3392 (1972).
30. Vasylechko, L. *et al*. The crystal structure of $NdGaO_3$ at 100 K and 293 K based on synchrotron data. *J. Alloys Compd.* **297,** 46–52 (2000).
31. Liao, Z., Huijben, M., Koster, G. & Rijnders, G. Uniaxial magnetic anisotropy induced low field anomalous anisotropic magnetoresistance in manganite thin films. *Appl. Phys. Lett. Mater.* **2,** 096112 (2014).
32. Ovsyannikov, S. V. *et al*. Perovskite-like Mn_2O_3: a path to new manganites. *Angew. Chem. Int. Ed.* **52,** 1494–1498 (2013).
33. Boschker, H. *et al*. Strong uniaxial in-plane magnetic anisotropy of (001)- and (011)-oriented $La_{0.67}Sr_{0.33}MnO_3$ thin films on $NdGaO_3$ substrates. *Phys. Rev. B* **79,** 214425 (2009).
34. Macke, S. *et al*. Element specific monolayer depth profiling. *Adv. Mater.* **26,** 6554–6559 (2014).
35. Park, J. H. *et al*. Magnetic properties at surface boundary of a half-metallic ferromagnet $La_{0.7}Sr_{0.3}MnO_3$. *Phys. Rev. Lett.* **81,** 1953–1956 (1998).
36. Huijben, M. *et al*. Critical thickness and orbital ordering in ultrathin $La_{0.7}Sr_{0.3}MnO_3$ films. *Phys. Rev. B* **78,** 094413 (2008).
37. Wang, B. M. *et al*. Oxygen-driven anisotropic transport in ultra-thin manganite films. *Nature Commun.* **4,** 2778 (2013).
38. Vailionis, A. *et al*. Misfit strain accommodation in epitaxial ABO_3 perovskites: lattice rotations and lattice modulations. *Phys. Rev. B* **83,** 064101 (2011).
39. Medarde, M. *et al*. High-pressure neutron-diffraction study of the metallization process in $PrNiO_3$. *Phys. Rev. B* **52,** 9248–9258 (1995).
40. Dong, S. *et al*. Highly anisotropic resistivities in the double-exchange model for strained manganites. *Phys. Rev. B* **82,** 159902 (2010).
41. Brataas, A., Kent, A. D. & Ohno, H. Current-induced torques in magnetic materials. *Nature Mater.* **11,** 372–381 (2012).
42. Brataasa, A., Bauer, G. E. W. & Kelly, P. J. Non-collinear magnetoelectronics. *Phys. Rep.* **427,** 157–255 (2006).
43. Kan, D. *et al*. Tuning magnetic anisotropy by interfacially engineering the oxygen coordination environment in a transition metal oxide. *Nature Mater.* http://dx.doi.org/10.1038/nmat4580 (2016).

Acknowledgements

Author contributions

Z.L. conceived the design and performed film growth and magnetic/transport measurements. Z.L., M.H., G.K., G.R. and Z.Z. performed data analysis and interpretation. N.G., S.V.A., J.V. and G.V.T. performed STEM and EDX measurements and analysis. S.M., G.K., R.J.G. and G.A.S. performed RXR measurements and analysis. Z.Z. and K.H. performed DFT calculations. All authors extensively discussed the results and were involved in writing of the manuscript.

Additional information

Supplementary information is available in the online version of the paper. Reprints and permissions information is available online at www.nature.com/reprints. Correspondence and requests for materials should be addressed to M.H.

Competing financial interests

The authors declare no competing financial interests.

Methods

LSMO thin films were grown on atomically flat NGO (110) substrates from a stoichiometric $La_{2/3}Sr_{1/3}MnO_3$ target by pulsed laser deposition using a KrF excimer laser operating at 248 nm. The atomically flat NGO substrate, as confirmed by atomic force microscopy (AFM), was obtained by buffered hydrofluoric acid chemical etching and subsequent annealing at 1,050 °C for 4 h (ref. 31). The laser fluence and repetition rate were 0.6 J cm^{-2} and 2 Hz, respectively. The oxygen partial pressure and substrate temperature were maintained at 0.2 mbar and 680 °C, respectively, during the growth. The growth process was monitored by reflection high-energy electron diffraction (RHEED), which confirmed the layer-by-layer characteristic growth.

Scanning transmission electron microscopy (STEM) was performed on the X-Ant-Em instrument at the University of Antwerp. Cross-sectional cuts of the samples along the [1$\bar{1}$0] and [001] directions were prepared using a FEI Helios 650 dual-beam focused ion beam (FIB) device. The 6 uc LSMO film was capped with a 10 nm STO layer grown at room temperature to prevent the LSMO ultrathin layer from damage during the preparation of the TEM cross-section specimen in both buffered and unbuffered cases. Satisfactory samples were prepared using very low energy ion beam thinning subsequent to protection of the sample surface by sputtering of a 10 nm carbon protection layer, followed be E-beam deposition of platinum as a first step to the FIB lamella preparation procedure. The electron microscope used consists of an FEI Titan G3 electron microscope equipped with an aberration corrector for the probe-forming lens, as well as a high-brightness gun and a Super-EDX 4-quadrant detector operated at 300 kV acceleration voltage for the EDX experiments and STEM-ADF and ABF imaging. The STEM convergence semi-angle used was 21 mrad, providing a probe size of ~0.8 Å. The collection semi-angles range from 11 to 29 mrad and 29–160 mrad for ABF and ADF imaging, respectively.

Magnetic and transport properties were measured by using a Quantum Design Vibration Sample Magnetometer (VSM) and a Physical Properties Measurement System (PPMS), respectively. The magnetization of the LSMO films was acquired by subtracting the paramagnetic signal of each NGO substrate (see Supplementary Fig. 14). The transport properties were analysed in a van der Pauw geometry, in which the resistances along the a- and b-axis were measured simultaneously.

The magneto-optical profile was measured using X-ray resonant magnetic reflectivity (XRMR; ref. 44). The XRMR experiments were performed using an in-vacuum 4-circle diffractometer at the Resonant Elastic and Inelastic X-ray Scattering (REIXS) beamline of the Canadian Light Source (CLS) in Saskatoon, Canada[45]. The beamline has a flux of 5×10^{12} photon s^{-1} and photon energy resolution $\Delta E/E$ of ~10^{-4}. The base pressure of the diffractometer chamber was kept below 10^{-9} torr. The samples were aligned with their surface normal in the scattering plane and measured at a temperature of 20 K. The measurements were carried out in the specular reflection geometry with several nonresonant photon energies as well as energies at the Mn L$_{2,3}$ resonance (~635–660 eV). For details about the magneto-optical profile extraction, see Supplementary Fig. 6.

A DFT-based tight-binding Hamiltonian was constructed to calculate the MAE of LSMO ultrathin films, $H(\mathbf{k}) + (\lambda/2)\sigma(\theta,\varphi) + \xi L \cdot S$, including exchange splitting λ and spin–orbit coupling ξ. The first term, $H(\mathbf{k})$, the paramagnetic tight-binding Hamiltonian, is constructed on a Wannier basis projected from DFT-calculated Bloch waves of LSMO near the Fermi level. The Wannier projection was performed with the Wien2Wannier package, employing Wannier90 for constructing maximally localized Wannier orbitals[46]. The second term, $(\lambda/2)\sigma(\theta,\varphi)$, leads to an exchange splitting λ for spins parallel and antiparallel to the (θ,φ) direction. We set $\lambda = 2$ eV, which is the typical exchange splitting in manganites[47]. The last term is the atomic spin orbit coupling of Mn d orbitals with $\xi = 0.05$ eV. A very fine k mesh (for example, $160 \times 160 \times 160$) was used to make sure that the total energy converges to an accuracy of 10^{-3} μeV.

References

44. Macke, S. & Goering, E. Magnetic reflectometry of heterostructures. *J. Phys. Condens. Matter* **26,** 363201 (2014).
45. Hawthorn, D. G. *et al*. An in-vacuum diffractometer for resonant elastic soft X-ray scattering. *Rev. Sci. Instrum.* **82,** 073104 (2011).
46. Zhong, Z., Toth, A. & Held, K. Theory of spin–orbit coupling at LaAlO$_3$/SrTiO$_3$ interfaces and SrTiO$_3$ surfaces. *Phys. Rev. B* **87,** 161102 (2013).
47. Yamasaki, A., Feldbacher, M., Yang, Y.-F., Andersen, O. K. & Held, K. Pressure-induced metal–insulator transition in LaMnO$_3$ is not of Mott-Hubbard type. *Phys. Rev. Lett.* **96,** 166401 (2006).